This article was downloaded by: *[Giesecke, Andre]*
On: *14 September 2010*
Access details: *Access Details: [subscription number 926952961]*
Publisher *Taylor & Francis*
Informa Ltd Registered in England and Wales Registered Number: 1072954 Registered office: Mortimer House, 37-41 Mortimer Street, London W1T 3JH, UK

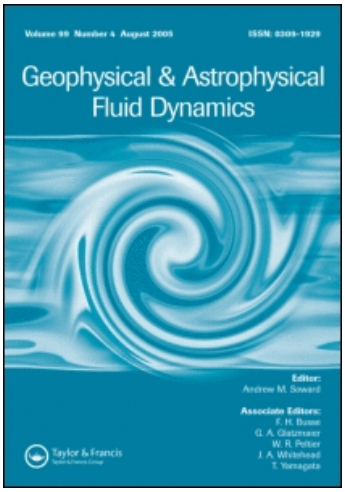

Geophysical & Astrophysical Fluid Dynamics
Publication details, including instructions for authors and subscription information:
http://www.informaworld.com/smpp/title~content=t713642804

Electromagnetic induction in non-uniform domains

A. Giesecke[a]; C. Nore[bc]; F. Stefani[a]; G. Gerbeth[a]; J. Léorat[d]; F. Luddens[be]; J. -L. Guermond[be]
[a] Forschungszentrum Dresden-Rossendorf, Dresden, Germany [b] Laboratoire d'Informatique pour la Mécanique et les Sciences de l'Ingénieur, CNRS, 91403 Orsay cedex, France [c] Institut Universitaire de France and Université Paris Sud 11, 91405 Orsay cedex, France [d] Luth, Observatoire de Paris-Meudon, place Janssen, 92195-Meudon, France [e] Department of Mathematics, Texas A&M University 3368 TAMU, College Station, TX 77843, USA

First published on: 14 September 2010

To cite this Article Giesecke, A. , Nore, C. , Stefani, F. , Gerbeth, G. , Léorat, J. , Luddens, F. and Guermond, J. -L.(2010) 'Electromagnetic induction in non-uniform domains', Geophysical & Astrophysical Fluid Dynamics,, First published on: 14 September 2010 (iFirst)
To link to this Article: DOI: 10.1080/03091929.2010.507202
URL: http://dx.doi.org/10.1080/03091929.2010.507202

PLEASE SCROLL DOWN FOR ARTICLE

Full terms and conditions of use: http://www.informaworld.com/terms-and-conditions-of-access.pdf

This article may be used for research, teaching and private study purposes. Any substantial or systematic reproduction, re-distribution, re-selling, loan or sub-licensing, systematic supply or distribution in any form to anyone is expressly forbidden.

The publisher does not give any warranty express or implied or make any representation that the contents will be complete or accurate or up to date. The accuracy of any instructions, formulae and drug doses should be independently verified with primary sources. The publisher shall not be liable for any loss, actions, claims, proceedings, demand or costs or damages whatsoever or howsoever caused arising directly or indirectly in connection with or arising out of the use of this material.

Geophysical and Astrophysical Fluid Dynamics
2010, 1–25, iFirst

Taylor & Francis
Taylor & Francis Group

Electromagnetic induction in non-uniform domains

A. GIESECKE*†, C. NORE‡§, F. STEFANI†, G. GERBETH†, J. LÉORAT¶, F. LUDDENS‡⊥ and J.-L. GUERMOND‡⊥

†Forschungszentrum Dresden-Rossendorf, Dresden, Germany
‡Laboratoire d'Informatique pour la Mécanique et les Sciences de l'Ingénieur, CNRS, BP 133, 91403 Orsay cedex, France
§Institut Universitaire de France and Université Paris Sud 11, 91405 Orsay cedex, France
¶Luth, Observatoire de Paris-Meudon, place Janssen, 92195-Meudon, France
⊥Department of Mathematics, Texas A&M University 3368 TAMU, College Station, TX 77843, USA

(*Received 31 March 2010; in final form 29 June 2010*)

Kinematic simulations of the induction equation are carried out for different setups suitable for the von-Kármán-Sodium (VKS) dynamo experiment. The material properties of the flow driving impellers are modeled by means of high-conducting and high-permeability disks in a cylindrical volume filled with a conducting fluid. Two entirely different numerical codes are mutually validated by showing quantitative agreement on Ohmic decay and kinematic dynamo problems using various configurations and physical parameters. Field geometry and growth rates are strongly modified by the material properties of the disks even if the disks are thin. In contrast the influence of external boundary conditions remains small. Utilizing a VKS like mean fluid flow and high-permeability disks yield a reduction of the critical magnetic Reynolds number Rm^c for the onset of dynamo action of the simplest non-axisymmetric field mode. However, this threshold reduction is not sufficient to fully explain the VKS experiment. We show that this reduction of Rm^c is influenced by small variations in the flow configuration so that the observed reduction may be changed with respect to small modifications of setup and properties of turbulence.

Keywords: Magnetohydrodynamics; Ohmic decay; Kinematic dynamo; Permeability; VKS dynamo

Downloaded By: [Giesecke, Andre] At: 22:12 14 September 2010

1. Introduction

Magnetic fields of galaxies, stars or planets are produced by dynamo action in a homogeneous medium in which a conducting fluid flow provides for generation of field energy. During the past decade the understanding of the field generation mechanism has considerably benefitted from the examination of dynamo action in the laboratory. However, realization of dynamo action in laboratories at least requires the magnetic Reynolds number $\mathrm{Rm} = UL/\eta$ (where U and L represent typical velocity and length scales and η denotes the magnetic diffusivity) to exceed a threshold of the

*Corresponding author. Email: a.giesecke@fzd.de

ISSN 0309-1929 print/ISSN 1029-0419 online © 2010 Taylor & Francis
DOI: 10.1080/03091929.2010.507202

order of $\mathrm{Rm}^c \sim 10...100$. From the parameter values of liquid sodium – the best known liquid conductor – at standard laboratory conditions ($\eta = 1/\mu_0\sigma \approx 0.1\,\mathrm{m}^2/\mathrm{s}$ and $L \approx 1\,\mathrm{m}$, where μ_0 is the vacuum permeability and σ the electrical conductivity) it becomes immediately obvious that self excitation of magnetic fields in the laboratory needs typical velocity magnitudes of $U \sim 10\,\mathrm{m/s}$, which is already quite demanding. Therefore, the first successful dynamo experiments performed by Lowes and Wilkinson (1963, 1968) utilized soft-iron material so that the magnetic diffusivity is reduced (this issue indeed deserves a specific study and is examined below) and the magnetic Reynolds number is (at least locally) increased. Although these experiments cannot be classified as hydromagnetic dynamos (no fluid flow and therefore no non-trivial backreaction of the field on a fluid motion is possible) they allowed the examination of distinct dynamical regimes manifested in steady, oscillating or reversing fields. It is interesting to note that these results did not initiate further numerical studies on induction in the presence of soft iron domains.

The effects of internal and external walls with finite permeability and conductivity have been examined in Avalos-Zuñiga *et al.* (2003, 2005) by analytically solving a one dimensional kinematic dynamo driven by an α-effect. A facilitation of dynamo action is obtained for increasing conductivity and/or permeability of given inner and outer walls. This threshold reduction is monotonous in the case of a stationary dynamo mode but non monotonous in the case of a time dependent dynamo due to dissipation from eddy currents induced within the container walls. The authors also assumed that a mean flow may increase the dynamo threshold due to additional dissipation. More recently, Roberts *et al.* (2010) performed nonlinear simulations in a sphere with a flow driven by the counter rotation of the two hemispherical parts of the outer sphere. Their setup and geometry are only roughly representative for the von-Kármán-Sodium (VKS) configuration (they also included an inner sphere made of a solid electrical insulator). They performed nonlinear simulations simultaneously varying permeability and conductivity of the external walls, applying thin wall conditions (where the wall thickness $h \to 0$ and the permeability $\mu_r \to \infty$ and conductivity $\sigma \to \infty$ so that the product $h\mu_r(h\sigma)$ remains finite). Only a few runs exhibit dynamo action and their results cannot yield any general conclusion about the influence of the wall permeability or conductivity on the dynamo threshold.

A possibility to increase the effective magnetic Reynolds number in fluid flow driven dynamo experiments arises from the addition of tiny ferrous particles to the fluid medium leading to a uniform enlargement of the relative permeability (Frick *et al.* 2002, Dobler *et al.* 2003). Since the amount of particles is limited so as to retain reasonable fluid properties, the maximum fluid permeability achievable by this technique is $\mu_r \approx 2$. The main effect found in the simulations of Dobler *et al.* (2003) was a reduced decay of the initial field but not a smaller threshold (essentially because of nonmonotonous behavior of the growth rate with respect to Rm).

Another type of ferromagnetic influence on dynamo action is observed in the VKS dynamo. In the VKS experiment a turbulent flow of liquid sodium is driven by two counterrotating impellers located at the opposite end caps of a cylindrical domain (Monchaux *et al.* 2007). Dynamo action is only obtained when the impellers are made of soft-iron with $\mu_r \sim 100$ (Verhille *et al.* 2010). Recently it has been shown in Giesecke *et al.* (2010b) that these soft-iron impellers essentially determine the geometry and the growth rates of the magnetic field by locally enhancing the magnetic Reynolds number and by enforcing internal boundary conditions for the magnetic field at the

Downloaded By: [Giesecke, Andre] At: 22:12 14 September 2010

material interfaces. We conjecture that non-homogeneous distributions of the material coefficients μ_r and σ may support dynamo action because gradients of μ_r and σ modify the induction equation by coupling toroidal and poloidal components of the magnetic fields which is essential for the occurrence of dynamo action. An example for this dynamo type has been presented in Busse and Wicht (1992) where it was shown that even a straight flow without shear over an (infinite) conducting plate with sinusoidal variation of the conductivity is able to produce dynamo action. However, an experimental realization of this setup would require either an unachievable large magnetic Reynolds number or rather large variations of the conductivity ($\gtrsim$ factor of 100 and with a mean value which should be of the order of the fluid conductivity). On the other hand, large permeability variations are more easily achievable experimentally, for instance the relative permeability of soft-iron alloys easily attains values of several thousands. Although these dynamos are of little astrophysical relevance the experiments of Lowes and Wilkinson and in particular the rich dynamical behavior of the VKS dynamo demonstrate the usefulness of such models.

The purpose of the present work is to validate the numerical tools necessary to establish a basic understanding of the influence of material properties on the induction process. Emphasis is given to the problem of free decay in cylindrical geometry where two disks characterized by high-conductivity/permeability and their thickness are inserted in the interior of a cylindrical container filled with a conducting fluid. To demonstrate the reliability of our results we use two different numerical approaches and show that both methods give results in agreement. The study is completed by an application of a mean flow as it occurs in the VKS experiment in combination with two high-permeability disks.

Downloaded By: [Giesecke, Andre] At: 22:12 14 September 2010

2. Induction equation in heterogenous domains

From Faraday's Law in combination with Ohm's Law, one immediately retrieves the induction equation that determines the temporal behavior of the magnetic flux density $\mathbf{B}$:

$$\frac{\partial \mathbf{B}}{\partial t} = \nabla \times \left(\mathbf{u} \times \mathbf{B} - \frac{1}{\mu_0 \sigma} \nabla \times \frac{\mathbf{B}}{\mu_r} \right), \tag{1}$$

where $\mathbf{u}$ denotes the flow velocity, σ the electric conductivity, μ_0 the vacuum permeability and μ_r the relative permeability. In case of spatially varying distributions of conductivity and permeability equation (1) can be rewritten in the form:

$$\begin{aligned} \frac{\partial \mathbf{B}}{\partial t} = {} & \nabla \times (\mathbf{u} \times \mathbf{B}) + \frac{1}{\mu_0 \mu_r \sigma} \nabla^2 \mathbf{B} + \frac{1}{\mu_0 \mu_r \sigma} \nabla \times (\nabla \ln \mu_r \times \mathbf{B}) \\ & - \frac{1}{\mu_0 \mu_r \sigma} (\nabla \ln \mu_r + \nabla \ln \sigma) \times (\nabla \ln \mu_r \times \mathbf{B}) + \frac{1}{\mu_0 \mu_r \sigma} (\nabla \ln \mu_r + \nabla \ln \sigma) \times (\nabla \times \mathbf{B}). \end{aligned} \tag{2}$$

The terms on the right-hand-side that involve gradients of μ_r and σ potentially couple the toroidal and poloidal field components which is known to be essential for the existence of a dynamo. The lack of symmetry between the terms containing $\nabla \mu_r$ and $\nabla \sigma$

indicates a distinct impact of σ and μ_r. This difference of behavior can also be anticipated by looking at the jump conditions that the electric and magnetic fields have to fulfill at material interfaces. At interfaces between materials 1 and 2 that exhibit a jump in conductivity σ and/or in relative permeability μ_r the normal component of the magnetic flux density is continuous whereas the tangential components exhibit a jump described by the ratio of the permeabilities. In case of conductivity discontinuities, the tangential components of the electric field are continuous and the normal component of the electric current is continuous. Mathematically these jump conditions are given by (see, e.g. Jackson 1975)

$$\begin{aligned} \mathbf{n}\cdot(\mathbf{B}_1-\mathbf{B}_2)=0, \quad \mathbf{n}\times\left(\frac{\mathbf{B}_1}{\mu_{r,1}}-\frac{\mathbf{B}_2}{\mu_{r,2}}\right)=0, \\ \mathbf{n}\cdot(\mathbf{j}_1-\mathbf{j}_2)=0, \quad \mathbf{n}\times(\mathbf{E}_1-\mathbf{E}_2)=0, \end{aligned} \tag{3}$$

where $\mathbf{n}$ denotes the unit vector in the normal direction on the interface between materials 1 and 2. If there is no contribution of the flow, the continuity of the normal current leads to the discontinuity of the normal electric field in the ratio of the conductivities. Although the transmission conditions (3) are standard, their dynamical consequences in flows at large Rm are largely unknown.

Downloaded By: [Giesecke, Andre] At: 22:12 14 September 2010

3. Numerical schemes

Two different numerical algorithms and codes are used for the numerical solution of problems involving the kinematic induction equation (1). The first one is a combined finite volume/boundary element method FV/BEM Stefani *et al*. (2009). It is a grid based approach which provides a flexible scheme that utilizes a local discretization and intrinsically maintains the solenoidal character of the magnetic field.

The second solution method is based on a Spectral/Finite Element approximation technique denoted as SFEMaNS for Spectral/Finite Elements for Maxwell and Navier-Stokes equations. Taking advantage of the cylindrical symmetry of the domains, Fourier modes are used in the azimuthal direction and finite elements are used in the meridional plane. For each Fourier mode this leads to independent two-dimensional-problems in the meridian plane.

3.1. *Hybrid finite volume/boundary element method*

We start with the induction equation in the conservative form

$$\frac{\partial\mathbf{B}}{\partial t}+\nabla\times\mathbf{E}=\mathbf{0}, \tag{4}$$

where the electric field $\mathbf{E}$ is given by

$$\mathbf{E}=-\mathbf{u}\times\mathbf{B}+\eta\nabla\times\frac{\mathbf{B}}{\mu_r} \tag{5}$$

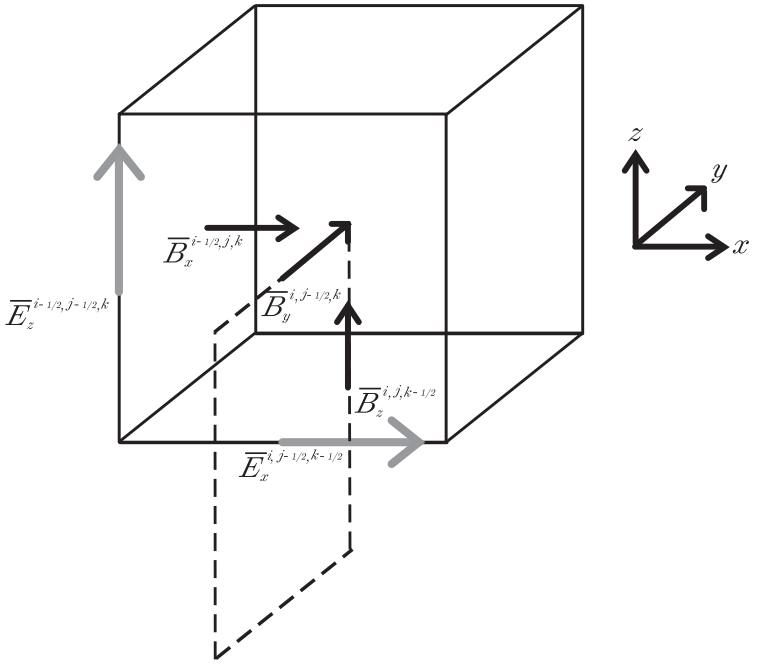

Figure 1. Localization of vector quantities on a grid cell *ijk* with the cell center located at (x_i, y_j, z_k). The dotted curve denotes the path along which the integration of **B** is executed for the computation of $\overline{E}_x^{i,j-1/2,k-1/2}$.

and $\eta = 1/\mu_0\sigma$ is the magnetic diffusivity. For the sake of simplicity we give a short sketch for the treatment of inhomogeneous conductivity and permeability only in Cartesian coordinates. The scheme can easily be adapted to different (orthogonal) coordinate systems (e.g. cylindrical or spherical coordinate system) making use of generalized coordinates (Stone and Norman 1992a,b).

In the finite volume scheme the grid representation of the magnetic field is given by a staggered collocation of the field components that are interpreted as an approximation of the (cell-)face average:

$$\overline{B}_x^{i-1/2,j,k} \approx \frac{1}{\Delta y \Delta z} \int_{\Gamma_{yz}} B_x(x_{i-1/2}, y, z) \mathrm{d}y \, \mathrm{d}z, \tag{6}$$

where the integration domain Γ corresponds to the surface of a single cell-face: $\Gamma_{yz} = [y_{j-1/2}, y_{j+1/2}] \times [z_{k-1/2}, z_{k+1/2}]$ (figure 1). A comparable definition is applied to the electric field which is localized at the center of a cell edge and which is defined as the line average (figure 1):

$$\overline{E}_x^{i,j-1/2,k-1/2} \approx \frac{1}{\Delta x} \int_{x^{i-1/2}}^{x^{i+1/2}} E_x(x, y_{j-1/2}, z_{k-1/2}) \mathrm{d}x. \tag{7}$$

Similar definitions hold for the components $\overline{B}_y^{i,j-1/2,k}$ and $\overline{B}_z^{i,j,-1/2}$, and for $\overline{E}_y^{i-1/2,j,k-1/2}$ and $\overline{E}_z^{i-1/2,j-1/2,k}$, respectively.

Downloaded By: [Giesecke, Andre] At: 22:12 14 September 2010

The finite volume discretization of the induction equation reads

$$\frac{\mathrm{d}}{\mathrm{d}t}\overline{B}_x^{\,i-1/2,j,k} = -\left(\frac{\overline{E}_z^{\,i-1/2,j+1/2,k}(t) - \overline{E}_z^{\,i-1/2,j-1/2,k}(t)}{\Delta y} - \frac{\overline{E}_y^{\,i-1/2,j,k+1/2}(t) - \overline{E}_y^{\,i-1/2,j,k-1/2}(t)}{\Delta z}\right) \tag{8}$$

and it can easily be shown that this approach preserves the $\nabla \cdot \mathbf{B}$ constraint for all times (to machine accuracy) if the initial field is divergence free.

3.1.1. Material coefficients. In the following we only discuss the treatment of the diffusive part of the electric field, $\mathbf{E} = \eta \nabla \times \mathbf{B}/\mu_r$ because the induction contribution ($\propto -\mathbf{u} \times \mathbf{B}$) does not involve the material properties and can be treated separately in the framework of an operator splitting scheme (see, e.g. Iskakov *et al.* 2004, Giesecke *et al.* 2008, Ziegler 1999). To obtain the computation directive for the electric field the magnetic field has to be integrated along a (closed path) around $\overline{E}_{x(,y,z)}$ at the edge of a grid cell (see dotted curve in figure 1).

$$\overline{E}_x \approx \frac{1}{\Gamma}\int_{\Gamma_{yz}} E_x \,\mathrm{d}A = \frac{1}{\Gamma}\int_{\Gamma_{yz}} \eta\left(\nabla \times \frac{\mathbf{B}}{\mu_\mathrm{r}}\right)\mathrm{d}A \approx \frac{\overline{\eta}}{\Delta y \Delta z}\int_{\partial\Gamma_{yz}} \frac{\mathbf{B}}{\mu_\mathrm{r}}\mathrm{d}\mathbf{l}, \tag{9}$$

where $\Gamma = \Delta y \Delta z$ is the surface surrounded by the path Γ_{yz} and $\overline{\eta}$ is the average diffusivity ($\eta = (\mu_0\sigma)^{-1}$) "seen" by the electric field. Unlike vectorial quantities the material coefficients are scalar quantities that are localized in the center of a grid cell. The consideration of spatial variations and/or jumps in conductivity respectively permeability is straightforward if corresponding averaging procedures for σ or μ_r are applied (Haber and Ascher 2001). For the component $\overline{E}_x$ the discretization of equation (9) leads to

$$\overline{E}_x^{\,i,j-1/2,k-1/2} = \overline{\eta}_{i,j-1/2,k-1/2}\left[\frac{1}{\Delta y}\left(\frac{\overline{B}_z^{\,i,j,-1/2}}{(\overline{\mu}_\mathrm{r})_{i,j,k-1/2}} - \frac{\overline{B}_z^{\,i,j-1,k-1/2}}{(\overline{\mu}_\mathrm{r})_{i,j-1,k-1/2}}\right) - \frac{1}{\Delta z}\left(\frac{\overline{B}_y^{\,i,j-1/2,k}}{(\overline{\mu}_\mathrm{r})_{i,j-1/2,k}} - \frac{\overline{B}_y^{\,i,j-1/2,k-1}}{(\overline{\mu}_\mathrm{r})_{i,j-1/2,k-1}}\right)\right]. \tag{10}$$

In equation (10), $\overline{\eta}_{i,j-1/2,k-1/2}$ represents the diffusivity that is seen by the electric field component $\overline{E}_x^{\,i,j-1/2,k-1/2}$ at the edge of the grid cell (ijk) and which is given by the arithmetic average of the diffusivity of the four adjacent cells:

$$\overline{\eta}_{i,j-1/2,k-1/2} = \frac{1}{4}\left(\eta_{i,j,k} + \eta_{i,j-1,k} + \eta_{i,j,k-1} + \eta_{i,j-1,k-1}\right). \tag{11}$$

Similarly, $\overline{\mu_\mathrm{r}}$ denotes the relative permeability that is seen by the magnetic field components ($\overline{B}_y$ and $\overline{B}_z$) at the interface between two adjacent grid cells. For instance, for the case considered in equation (10), μ_r is defined as follows:

$$\begin{aligned} \text{for } \overline{B}_y^{\,i,j-1/2,k}\text{:} \quad & (\overline{\mu}_\mathrm{r})_{i,j-1/2,k} = \frac{2(\mu_\mathrm{r})_{i,j,k}(\mu_\mathrm{r})_{i,j-1,k}}{(\mu_\mathrm{r})_{i,j,k} + (\mu_\mathrm{r})_{i,j-1,k}}, \\ \text{for } \overline{B}_z^{\,i,j,-1/2}\text{:} \quad & (\overline{\mu}_\mathrm{r})_{i,j,k-1/2} = \frac{2(\mu_\mathrm{r})_{i,j,k}(\mu_\mathrm{r})_{i,j,k-1}}{(\mu_\mathrm{r})_{i,j,k} + (\mu_\mathrm{r})_{i,j,k-1}}. \end{aligned} \tag{12}$$

Downloaded By: [Giesecke, Andre] At: 22:12 14 September 2010

For the computation of $\overline{E}_y^{\,i-1/2,j,k-1/2}$ and $\overline{E}_z^{\,i-1/2,j-1/2,k}$ equations (11) and (12) have to be adjusted according to the localization and the field components involved. Applying the averaging rules (11) and (12) to the computation of the "diffusive" part of the electric field results in a scheme that intrinsically fulfills the jump conditions (3) at material interfaces. The scheme is robust and simple to implement, however, the averaging procedure results in an artificial smoothing of parameter jumps at interfaces and in concave corners additional difficulties might occur caused by ambiguous expressions for μ_r. Furthermore, in the simple realization presented above, the parameter range is restricted. For larger jumps of μ_r or σ a more careful treatment of the discontinuities at the material interfaces is necessary which would require a more elaborate field reconstruction that makes use of slope limiters.

Downloaded By: [Giesecke, Andre] At: 22:12 14 September 2010

3.1.2. Boundary conditions. In numerical simulations of laboratory dynamo action insulating boundary conditions are often simplified by assuming vanishing tangential fields (VTF, sometimes also called pseudo vacuum condition). In fact, a restriction of the boundary magnetic field to its normal component resembles an artificial but numerically convenient setup where the exterior of the computational domain is characterized by an infinite permeability. VTF boundary conditions usually overestimate the field growth rates in many dynamo problems. Therefore, a more elaborate treatment of the field behavior at the boundary is recommended which is nontrivial in non-spherical coordinate systems. Insulating domains are characterized by a vanishing current $\mathbf{j} \propto \nabla \times \mathbf{B} = \mathbf{0}$ so that $\mathbf{B}$ can be expressed as the gradient of a scalar field Φ (assuming that the insulating domain is simply connected) which fulfills the Laplace equation:

$$\mathbf{B} = -\nabla\Phi \quad \text{with} \quad \nabla^2\Phi = 0, \quad \Phi \to \mathrm{O}(r^{-2}) \quad \text{for } r \to \infty. \tag{13}$$

Integrating $\nabla^2\Phi = 0$ and adoption of Green's 2nd theorem leads to

$$\Phi(\mathbf{r}) = 2\int_\Gamma G(\mathbf{r},\mathbf{r}')\underbrace{\frac{\partial\Phi(\mathbf{r}')}{\partial n}}_{-B^{\mathrm{n}}(\mathbf{r}')} - \Phi(\mathbf{r}')\frac{\partial G(\mathbf{r},\mathbf{r}')}{\partial n}\mathrm{d}\Gamma(\mathbf{r}'), \tag{14}$$

where $G(\mathbf{r},\mathbf{r}') = -(4\pi|\mathbf{r}-\mathbf{r}'|)^{-1}$ is the Greens function (with $\nabla^2 G(\mathbf{r},\mathbf{r}') = -\delta(\mathbf{r}-\mathbf{r}')$) and $\partial/\partial n$ is the normal derivative on the surface element $\mathrm{d}\Gamma$ so that $\partial_n\Phi = -B^{\mathrm{n}}$ yields the normal component of $\mathbf{B}$ on $\mathrm{d}\Gamma$. The tangential components of the magnetic field at the boundary $B^{\tau} = \mathbf{e}_\tau \cdot \mathbf{B} = -\mathbf{e}_\tau \cdot \nabla\Phi(\mathbf{r})$ are computed from equation (14) as follows:

$$B^{\tau} = 2\int_\Gamma \mathbf{e}_\tau \cdot \left(\Phi(\mathbf{r}')\nabla_r\frac{\partial G(\mathbf{r},\mathbf{r}')}{\partial n} + B^{\mathrm{n}}(\mathbf{r}')\nabla_r G(\mathbf{r},\mathbf{r}')\right)\mathrm{d}\Gamma(\mathbf{r}'), \tag{15}$$

where $\mathbf{e}_\tau$ represents a tangential unit vector on the surface element $\mathrm{d}\Gamma(\mathbf{r}')$. In fact, there are two orthogonal tangential directions on the boundary and equation (15) is valid independently for both orientations. After the subdivision of the surface Γ in boundary elements Γ_j with $\Gamma = \cup\Gamma_j$ the approximate potential $\Phi_i = \Phi(\mathbf{r_i})$ and the tangential field

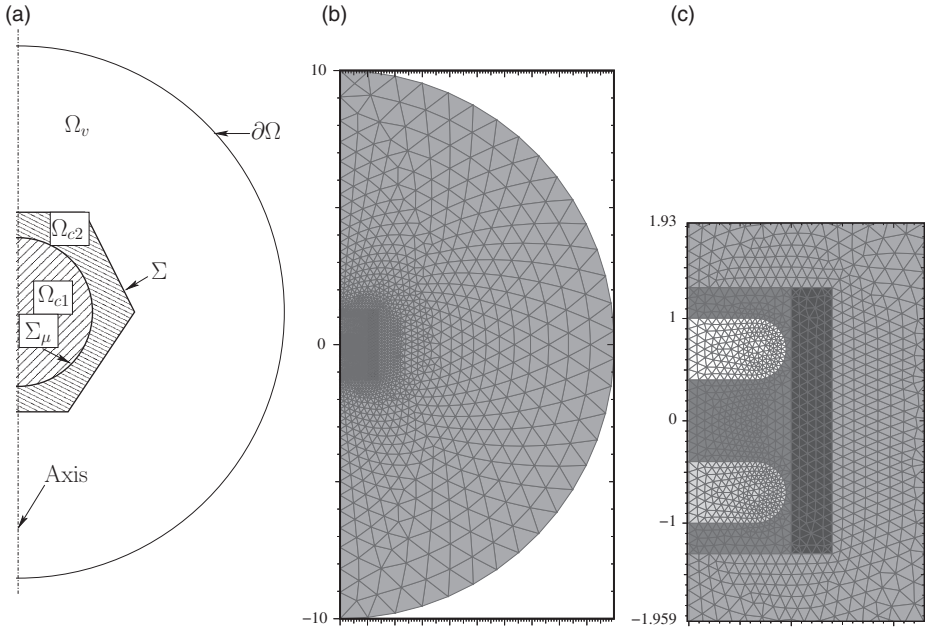

Figure 2. Example of a computational domain Ω with various boundaries: (a) sketch with arbitrary axisymmetrical domains showing the conducting domain Ω_c (shaded regions) and the vacuum Ω_v (non-shaded domain) with the interfaces Σ_μ and Σ, (b) meridian triangular mesh used in section 4 with disks of $d=0.6$ thickness with SFEMaNS (1 point out of 4 has been represented), (c) zoom of (b).

$B_i^\tau = B^\tau(\mathbf{r}_i) = -\mathbf{e}_\tau \cdot (\nabla \Phi_i)$ in discretized form are given by

$$\begin{aligned} \frac{1}{2}\Phi_i &= -\sum_j \left(\int_{\Gamma_j} \frac{\partial G}{\partial n}(\mathbf{r}_i, \mathbf{r}') \mathrm{d}\Gamma'_j \right) \Phi_j, -\sum_j \left(\int_{\Gamma_j} G(\mathbf{r}_i, \mathbf{r}') \mathrm{d}\Gamma'_j \right) B_j^{\mathrm{n}} \\ B_i^\tau &= \sum_j \left(\int_{\Gamma_j} 2\mathbf{e}_\tau \cdot \nabla_r \frac{\partial G}{\partial n}(\mathbf{r}_i, \mathbf{r}') \mathrm{d}\Gamma'_j \right) \Phi_j + \sum_j \left(\int_{\Gamma_j} 2\mathbf{e}_\tau \cdot \nabla_r G(\mathbf{r}_i, \mathbf{r}') \mathrm{d}\Gamma'_j \right) B_j^{\mathrm{n}}. \end{aligned} \tag{16}$$

The system of equations (16) gives a linear, non local relation for the tangential field components at the boundary in terms of the normal components and closes the problem of magnetic induction in finite (connected) domains with insulating boundaries (Iskakov and Dormy 2005). A more detailed description of the scheme can be found in Giesecke *et al.* (2008).

3.2. *Spectral/Finite Elements for Maxwell equations*

The conducting part of the computational domain is denoted by Ω_c, the non-conducting part (vacuum) is denoted Ω_v, and we set $\Omega := \Omega_c \cup \Omega_v$. We use the subscript c for the conducting part and v for the vacuum. We assume that Ω_c is partitioned into subregions $\Omega_{c1}, \ldots, \Omega_{cN}$, so that the magnetic permeability in each subregion Ω_{ci}, say μ^{ci}, is smooth. We denote by Σ_μ, the interface between all the conducting subregions. We denote by Σ, the interface between Ω_c and Ω_v. A sketch of the computational domain is displayed in figure 2(a).

Downloaded By: [Giesecke, Andre] At: 22:12 14 September 2010

The electric field $\mathbf{E}$ and magnetic field $\mathbf{H}$ in Ω_c and Ω_v solve the following system:

$$\frac{\partial(\mu^c\mathbf{H}^c)}{\partial t} = -\nabla\times\mathbf{E}^c, \quad \frac{\partial(\mu^v\mathbf{H}^v)}{\partial t} = -\nabla\times\mathbf{E}^v, \tag{17}$$

$$\nabla\cdot(\mu^c\mathbf{H}^c) = 0, \quad \nabla\cdot(\mu^v\mathbf{H}^v) = 0, \tag{18}$$

$$\mathbf{E}^{\mathbf{c}} = -\mathbf{u}\times\mu^c\mathbf{H}^{\mathbf{c}} + \frac{1}{\sigma}\nabla\times\mathbf{H}^{\mathbf{c}}, \quad \nabla\times\mathbf{H}^v = \mathbf{0} \tag{19}$$

and the following transmission conditions hold across Σ_μ and Σ:

$$\mathbf{H}^{ci}\times\mathbf{n}^{ci} + \mathbf{H}^{cj}\times\mathbf{n}^{cj} = \mathbf{0}, \quad \mathbf{H}^c\times\mathbf{n}^c + \mathbf{H}^v\times\mathbf{n}^v = \mathbf{0}, \tag{20}$$

$$\mu^{ci}\mathbf{H}^{ci}\cdot\mathbf{n}^{ci} + \mu^{cj}\mathbf{H}^{cj}\cdot\mathbf{n}^{cj} = 0, \quad \mu^c\mathbf{H}^c\cdot\mathbf{n}^c + \mu^v\mathbf{H}^v\cdot\mathbf{n}^v = 0, \tag{21}$$

$$\mathbf{E}^{ci}\times\mathbf{n}^{ci} + \mathbf{E}^{cj}\times\mathbf{n}^{cj} = \mathbf{0}, \quad \mathbf{E}^c\times\mathbf{n}^c + \mathbf{E}^v\times\mathbf{n}^v = \mathbf{0}, \tag{22}$$

where $\mathbf{n}^c$ (resp. $\mathbf{n}^v$) is the unit outward normal on Σ, i.e. $\mathbf{n}^c$ points from Ω_c to Ω_v (resp. from Ω_v to Ω_c), and $\mathbf{n}^{ci}$ is the unit normal on Σ_μ, i.e. $\mathbf{n}^{ci}$ points from Ω_{ci} to Ω_{cj}.

Downloaded By: [Giesecke, Andre] At: 22:12 14 September 2010

3.2.1. Weak formulation. The finite element solution is computed by solving a weak form of the system (17)–(22). We proceed as follows in Ω_{ci}. Multiplying the induction equation in Ω_{ci} by a test-function $\mathbf{b}$, integrating over Ω_{ci}, integrating by parts and using (19) gives

$$\begin{aligned}
0 &= \int_{\Omega_{ci}} \frac{\partial(\mu^{ci}\mathbf{H}^{ci})}{\partial t}\cdot\mathbf{b} + \int_{\Omega_{ci}} \nabla\times\mathbf{E}^{ci}\cdot\mathbf{b} \\
&= \int_{\Omega_{ci}} \frac{\partial(\mu^{ci}\mathbf{H}^{ci})}{\partial t}\cdot\mathbf{b} + \int_{\Omega_{ci}} \mathbf{E}^{ci}\cdot\nabla\times\mathbf{b} + \int_{\partial\Omega_{ci}} (\mathbf{n}^{ci}\times\mathbf{E}^{ci})\cdot\mathbf{b} \\
&= \int_{\Omega_{ci}} \frac{\partial(\mu^{ci}\mathbf{H}^{ci})}{\partial t}\cdot\mathbf{b} + \int_{\Omega_{ci}} \left(-\mathbf{u}\times\mu^{ci}\mathbf{H}^{ci} + \frac{1}{\sigma}\nabla\times\mathbf{H}^{ci}\right)\cdot\nabla\times\mathbf{b} + \int_{\partial\Omega_{ci}} \mathbf{E}^{ci}\cdot(\mathbf{b}\times\mathbf{n}^{ci}).
\end{aligned} \tag{23}$$

Note that, in the weak formulation, the variable of integration is omitted. We proceed slightly differently in Ω_v. From (19) we infer that $\mathbf{H}^v$ is a gradient for a simply connected vacuum, i.e. $\mathbf{H}^v = \nabla\phi^v$. Thus taking a test-function of the form $\nabla\psi$, where ψ is a scalar potential defined on Ω_v, multiplying (17) by $\nabla\psi$ and integrating over Ω_v, we obtain

$$\int_{\Omega_v} \frac{\partial(\mu^v\nabla\phi^v)}{\partial t}\cdot\nabla\psi + \int_\Sigma \mathbf{E}^v\cdot\nabla\psi\times\mathbf{n}^v + \int_{\partial\Omega} \mathbf{E}^v\cdot\nabla\psi\times\mathbf{n}^v = 0. \tag{24}$$

We henceforth assume that $\mathbf{a} := \mathbf{E}_{|\partial\Omega}$ is a data. Since only the tangential parts of the electric field are involved in the surface integrals in (23) and (24), we can use the jump conditions (22) to write

$$\int_{\Sigma_\mu} \mathbf{E}^{ci}\cdot\mathbf{b}\times\mathbf{n}^{ci} = \int_{\Sigma_\mu} \{\mathbf{E}^c\}\cdot\mathbf{b}\times\mathbf{n}^{ci}, \quad \int_\Sigma \mathbf{E}^v\cdot\nabla\psi\times\mathbf{n}^v = \int_\Sigma \mathbf{E}^c\cdot\nabla\psi\times\mathbf{n}^v,$$

where $\{\mathbf{E}^c\}$ is defined on Σ_μ by $\{\mathbf{E}^c\} = \frac{1}{2}\left(\mathbf{E}^{ci} + \mathbf{E}^{cj}\right)$. We now add (23) (for $i = 1, \ldots, N$) and (24) to obtain

$$\int_{\Omega_c} \frac{\partial(\mu^c \mathbf{H}^c)}{\partial t} \cdot \mathbf{b} + \int_{\Omega_v} \frac{\partial(\mu^v \nabla\phi^v)}{\partial t} \cdot \nabla\psi + \int_{\cup_{i=1}^N \Omega_{ci}} \left(\frac{1}{\sigma}\nabla \times \mathbf{H}^{ci} - \mathbf{u} \times \mu^{ci}\mathbf{H}^{ci}\right) \cdot \nabla \times \mathbf{b}$$
$$+ \int_{\Sigma_\mu} \{\mathbf{E}^c\} \cdot [\![\mathbf{b} \times \mathbf{n}]\!] + \int_{\Sigma} \mathbf{E}^c \cdot (\mathbf{b} \times \mathbf{n}^c + \nabla\psi \times \mathbf{n}^v) = -\int_{\partial\Omega} \mathbf{a} \cdot \nabla\psi \times \mathbf{n}^v,$$

where we have set $[\![\mathbf{b} \times \mathbf{n}]\!] := (\mathbf{b}_i \times \mathbf{n}^{ci} + \mathbf{b}_j \times \mathbf{n}^{cj})$ with $\mathbf{b}_i := \mathbf{b}|_{\Omega_{ci}}$ and $\mathbf{b}_j := \mathbf{b}|_{\Omega_{cj}}$. We finally get rid of $\mathbf{E}^c$ by using Ohm's law in the conductor:

$$\int_{\Omega_c} \frac{\partial(\mu^c \mathbf{H}^c)}{\partial t} \cdot \mathbf{b} + \int_{\Omega_v} \frac{\partial(\mu^v \nabla\phi^v)}{\partial t} \cdot \nabla\psi + \int_{\cup_{i=1}^N \Omega_{ci}} \left(\frac{1}{\sigma}\nabla \times \mathbf{H}^{ci} - \mathbf{u} \times \mu^{ci}\mathbf{H}^{ci}\right) \cdot \nabla \times \mathbf{b}$$
$$+ \int_{\Sigma_\mu} \left\{\frac{1}{\sigma}\nabla \times \mathbf{H}^c - \mathbf{u} \times \mu^c\mathbf{H}^c\right\} \cdot [\![\mathbf{b} \times \mathbf{n}]\!] + \int_{\Sigma} \left(\frac{1}{\sigma}\nabla \times \mathbf{H}^c - \mathbf{u} \times \mu^c\mathbf{H}^c\right) \cdot (\mathbf{b} \times \mathbf{n}^c + \nabla\psi \times \mathbf{n}^v)$$
$$= -\int_{\partial\Omega} \mathbf{a} \cdot \nabla\psi \times \mathbf{n}^v. \tag{25}$$

This formulation is the starting point for the finite element discretization.

3.2.2. Space discretization. As already mentioned, SFEMaNS takes advantage of the cylindrical symmetry. We denote Ω_v^{2d} and Ω_{ci}^{2d} the meridian sections of Ω_v and Ω_{ci}, respectively. These sections are meshed using quadratic triangular meshes (we assume that Ω_v^{2d} and the sub-domains $\Omega_{c1}^{2d} \ldots \Omega_{cN}^{2d}$ have piecewise quadratic boundaries). We denote $\{F_h^v\}_{h>0}, \{F_h^{c1}\}_{h>0} \ldots \{F_h^{cN}\}_{h>0}$ the corresponding regular families of non-overlapping quadratic triangular meshes, where h denotes the typical size of a mesh element. Figures 2(b) and (c) display a meridian triangular mesh used in section 4 with disks of thickness $d = 0.6$ (see section 4 for details). We use the same mesh strategy for all the sub-domains. We can use refinement, but the ratio between the maximum size of an element and the minimum one is of order 1. For every triangle K in the mesh we denote $T_K : \hat{K} \longrightarrow K$ the quadratic transformation that maps the reference triangle $\hat{K} := \{(\hat{r}, \hat{z}) \in R^2,\ 0 \le \hat{r},\ 0 \le \hat{z},\ \hat{r} + \hat{z} \le 1\}$ to K. Given ℓ_H and ℓ_ϕ two integers in $\{1, 2\}$ with $\ell_\phi \ge \ell_H$ we first define the meridian finite element spaces

$$\mathbf{X}_h^{H,2d} := \left\{\mathbf{b}_h \in \mathbf{L}^1(\Omega_c)/\mathbf{b}_h|_{\Omega_{ci}} \in C^0(\overline{\Omega}_{ci})\ \forall i = 1, \ldots, N,\ \mathbf{b}_h(T_K) \in P_{\ell_H},\ \forall K \in \cup_{i=1}^N F_h^{ci}\right\},$$
$$X_h^{\phi,2d} := \left\{\psi_h \in C^0(\overline{\Omega}_v)/\psi_h(T_K) \in P_{\ell_\phi}\ \forall K \in F_h^v\right\},$$

where $\mathbb{P}_k$ denotes the set of (scalar or vector valued) bivariate polynomials of total degree at most k. Then, using the complex notation $\mathrm{i}^2 = -1$, the magnetic field and the scalar potential are approximated in the following spaces:

$$\mathbf{X}_h^H := \left\{\mathbf{b}_h = \sum_{m=-M}^{M} \mathbf{b}_h^m(r, z)\mathrm{e}^{\mathrm{i}m\theta} \quad \forall m = 0, \ldots, M,\ \mathbf{b}_h^m \in \mathbf{X}_h^{H,2d} \text{ and } \mathbf{b}_h^m = \overline{\mathbf{b}_h^{-m}}\right\},$$
$$X_h^\phi := \left\{\psi_h = \sum_{m=-M}^{M} \psi_h^m(r, z)\mathrm{e}^{\mathrm{i}m\theta} \quad \forall m = 0, \ldots, M,\ \psi_h^m \in \mathbf{X}_h^{H,2d} \text{ and } \psi_h^m = \overline{\psi_h^{-m}}\right\},$$

where $M + 1$ is the maximum number of complex Fourier modes.

Downloaded By: [Giesecke, Andre] At: 22:12 14 September 2010

3.2.3. Time discretization. We approximate the time derivatives using the second-order Backward Difference Formula (BDF2). The terms that are likely to mix Fourier modes are made explicit. Let Δt be the time step and set $t^n := n\Delta t$, $n \geqslant 0$. After proper initialization at t^0 and t^1, the algorithm proceeds as follows. For $n \geqslant 1$ we set

$$\mathbf{H}^* = 2\mathbf{H}^{c,n} - \mathbf{H}^{c,n-1} \quad \text{and} \quad \begin{cases} D\mathbf{H}^{c,n+1} := \frac{1}{2}\big(3\mathbf{H}^{c,n+1} - 4\mathbf{H}^{c,n} + \mathbf{H}^{c,n-1}\big), \\ D\phi^{v,n+1} := \frac{1}{2}\big(3\phi^{v,n+1} - 4\phi^{v,n} + \phi^{v,n-1}\big), \end{cases}$$

and the discrete fields $\mathbf{H}^{c,n+1} \in \mathbf{X}_h^H$ and $\phi^{v,n+1} \in X_h^\phi$ are computed so that the following holds for all $\mathbf{b} \in \mathbf{X}_h^H$, $\psi \in X_h^\phi$:

$$L\big((\mathbf{H}^{c,n+1}, \phi^{v,n+1}), (\mathbf{b}, \psi)\big) = R(\mathbf{b}, \psi), \tag{26}$$

where the linear for $\mathcal{R}$ is defined by

$$R(\mathbf{b}, \psi) = -\int_{\partial\Omega} \mathbf{a} \cdot \nabla\psi \times \mathbf{n}^v + \int_{\Omega_c} \mathbf{u} \times \mu^c \mathbf{H}^* \cdot \nabla \times \mathbf{b} + \int_{\Sigma_\mu} \{\mathbf{u} \times \mu^c \mathbf{H}^*\} \cdot [\![\mathbf{b} \times \mathbf{n}]\!] + \int_{\Sigma} \mathbf{u} \times \mu^c \mathbf{H}^* \cdot (\mathbf{b} \times \mathbf{n}^c + \nabla\psi \times \mathbf{n}^v),$$

the bilinear form $\mathcal{L}$ is defined by

$$\begin{aligned} &L\big((\mathbf{H}^{c,n+1}, \phi^{v,n+1}), (\mathbf{b}, \psi)\big) \\ &\quad := \int_{\Omega_c} \mu^c \frac{D\mathbf{H}^{c,n+1}}{\Delta t} \cdot \mathbf{b} + \int_{\Omega_v} \mu^v \frac{\nabla D\phi^{v,n+1}}{\Delta t} \cdot \nabla\psi + \int_{\Omega_c} \frac{1}{\sigma} \nabla \times \mathbf{H}^{c,n+1} \cdot \nabla \times \mathbf{b} \\ &\qquad + g\big((\mathbf{H}^{c,n+1}, \phi^{v,n+1}), (\mathbf{b}, \psi)\big) + \int_{\Sigma_\mu} \left\{\frac{1}{\sigma} \nabla \times \mathbf{H}^{c,n+1}\right\} \cdot [\![\mathbf{b} \times \mathbf{n}]\!] \\ &\qquad + \int_{\Sigma} \frac{1}{\sigma} \nabla \times \mathbf{H}^{c,n+1} \cdot (\mathbf{b} \times \mathbf{n}^c + \nabla\psi \times \mathbf{n}^v) \end{aligned}$$

and the bilinear form g is defined by

$$\begin{aligned} g((\mathbf{H}_h, \psi_h), (\mathbf{b}_h, \psi_h)) := \beta_1 h_F^{-1} \int_{\Sigma_\mu} \big(\mathbf{H}_{h,1} \times \mathbf{n}_1^c + \mathbf{H}_{h,2} \times \mathbf{n}_2^c\big) \cdot \big(\mathbf{b}_{h,1} \times \mathbf{n}_1^c + \mathbf{b}_{h,2} \times \mathbf{n}_2^c\big) \\ + \beta_2 h_F^{-1} \int_{\Sigma} (\mathbf{H}_h \times \mathbf{n}^c + \nabla\psi_h \times \mathbf{n}^v) \cdot (\mathbf{b}_h \times \mathbf{n}^c + \nabla\psi_h \times \mathbf{n}^v), \end{aligned}$$

where h_F denotes the typical size of $\partial K \cup \Sigma_\mu$ or $\partial K \cup \Sigma$ for all K in the mesh such that $\partial K \cup \Sigma_\mu$ or $\partial K \cup \Sigma$ is not empty. The constant coefficients β_1 and β_2 are chosen to be of order 1. The purpose of the bilinear form g is to penalize the tangential jumps $[[\mathbf{H}^{c,n+1} \times \mathbf{n}]]$ and $\mathbf{H}^{c,n+1} \times \mathbf{n}^c + \nabla\psi^{v,n+1} \times \mathbf{n}^v$, so that they converge to zero when the mesh-size goes to zero.

3.2.4. Addition of a magnetic pressure. The above time-marching algorithm is convergent on finite time intervals but may fail to provide a convergent solution in a steady state regime since errors may accumulate on the divergence of the magnetic induction. We now detail the technique which is employed to control the divergence of $\mathbf{B}^c$ on arbitrary time intervals.

Downloaded By: [Giesecke, Andre] At: 22:12 14 September 2010

To avoid non-convergence properties that could occur in non-smooth domains and discontinuous material properties, we have designed a non standard technique inspired from Bonito and Guermond (2010) to control $\nabla \cdot \mathbf{B}$. We replace the induction equation in Ω_c by the following:

$$\frac{\partial(\mu^c \mathbf{H}^c)}{\partial t} = -\nabla \times \mathbf{E}^c + \mu^c \nabla p^c, \quad (-\Delta_0)^\alpha p^c = \nabla \cdot \mu^c \mathbf{H}^c, \quad p^c|_{\partial\Omega_c} = 0, \tag{27}$$

where α is a real parameter, Δ_0 is the Laplace operator with zero boundary condition on Ω_c, and p^c is a new scalar unknown. A simple calculation shows that $p^c = 0$ if the initial magnetic induction is solenoidal; hence, (27) enforces $\nabla \cdot \mu^c \mathbf{H}^c = 0$. Taking $\alpha = 0$ amounts to penalizing $\nabla \cdot \mu^c \mathbf{H}^c$ in $\mathbf{L}^2(\Omega_c)$, which turns out to be non-convergent with Lagrange finite elements when the boundary of Ω_c is not smooth, (see Costabel (1991) for details). The mathematical analysis shows that the method converges with Lagrange finite elements when $\alpha \in (\frac{1}{2}, 1)$. In practice we take $\alpha = 0.7$.

We introduce new finite elements spaces to approximate the new scalar unknown p^c

$$X_h^{p,2d} := \left\{ p_h \in L^1(\Omega_c) / p_h \in C^0(\overline{\Omega_c}),\ p_h(T_K) \in P_{\ell_p}\ \forall K \in \cup_{i=1}^N F_h^{ci},\ p_h = 0 \text{ on } \partial\Omega_c \right\},$$

$$X_h^p := \left\{ p = \sum_{m=-M}^{M} p^m(r,z) \mathrm{e}^{\mathrm{i}m\theta} / \forall m = 1 \ldots, M,\ p^m \in X_h^{p,2d} \text{ and } p^m = \overline{p^{-m}} \right\}.$$

Here ℓ_p is an integer in $\{1, 2\}$. The final form of the algorithm is the following: after proper initialization, we solve for $\mathbf{H}^{c,n+1} \in \mathbf{X}_h^H$, $\phi^{v,n+1} \in X_h^\phi$ and $p^{n+1} \in X_h^p$ so that the following holds for all $\mathbf{b} \in \mathbf{X}_h^H$, $\psi \in X_h^\phi$, $q \in X_h^p$:

$$L\big((\mathbf{H}^{c,n+1}, \phi^{v,n+1}), (\mathbf{b}, \psi)\big) + D\big((\mathbf{H}^{c,n+1}, p^{c,n+1}, \phi^{v,n+1}), (\mathbf{b}, q, \psi)\big) + P(\phi^{v,n+1}, \psi) = R(\mathbf{b}, \psi) \tag{28}$$

with

$$D((\mathbf{H}, p, \phi), (\mathbf{b}, q, \psi)) := \sum_{i=1}^{N} \int_{\Omega_{ci}} \left(\mu^c \mathbf{b} \cdot \nabla p - \mu^c \mathbf{H} \cdot \nabla q + h^{2\alpha} \nabla \cdot \mu^c \mathbf{H}\, \nabla \cdot \mu^c \mathbf{b} + h^{2(1-\alpha)} \nabla p \cdot \nabla q \right), \tag{29}$$

where h denotes the typical size of a mesh element. The term $\sum_{i=1}^N \int_{\Omega_{ci}} h^{2\alpha} \nabla \cdot \mu^c \mathbf{H}^{c,n+1} \nabla \cdot \mu^c \mathbf{b}$ is a stabilization quantity which is added in to have discrete well-posedness of the problem irrespective of the polynomial degree of the approximation for p^c. The additional stabilizing bilinear form $\mathcal{P}$ is defined by

$$P(\phi, \psi) = \int_{\Omega_v} \nabla\phi \cdot \nabla\psi - \int_{\partial\Omega_v} \psi \mathbf{n} \cdot \nabla\phi.$$

This bilinear form is meant to help ensure that $\Delta\phi^{v,n+1} = 0$ for all times.

3.2.5. Taking advantage of the cylindrical symmetry for Maxwell and Navier–Stokes equations. SFEMaNS is a fully nonlinear code integrating the coupled Maxwell and Navier–Stokes equations (Guermond *et al.* 2007, 2009). As mentioned above, any term that could mix different Fourier modes has been made explicit. Owing to this property, there are $M+1$ independent linear systems to solve at each time step ($M+1$ being the

Downloaded By: [Giesecke, Andre] At: 22:12 14 September 2010

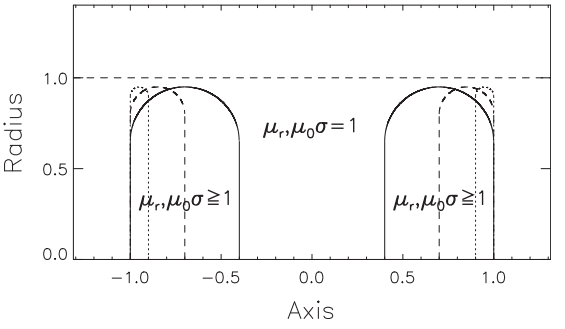

Figure 3. Sketch of the set up. Two disks with thickness $d=0.6, 0.3, 01$ (solid, dashed, dotted curve) are introduced in a cylinder with height $H=2.6$ and radius $R=1.4$. In all runs the location of the backside of each disk is fixed at $z=\pm1$. At the outer disk edge a circular shape is applied with a curvature radius corresponding to half of the disk thickness. The radial extension of the disks is fixed and given by $R_{\text{disk}}=0.95$. The dashed horizontal line denotes the inner boundary that separates the dynamical active region from the stagnant outer layer in the runs with $\text{Rm}>0$ (Section 5).

Downloaded By: [Giesecke, Andre] At: 22:12 14 September 2010

maximum number of complex Fourier modes). This immediately provides a parallelization strategy. In practice, we use one processor per Fourier mode. The computation of the nonlinear terms in the right-hand side is done using a parallel Fast Fourier Transform. Note that, in the present article, we use only the kinematic part of the code with an axisymmetric steady flow. A typical time step is $\Delta t=0.01$ and a typical mesh size is $h=1/80$. When necessary, the mesh is refined in the vicinity of the curved interface Σ_μ so that we have $h=1/400$ locally.

4. Ohmic decay in heterogenous domains

The inspection of equations (3) shows that even in the absence of flow, heterogeneous domains can lead to non-trivial Ohmic decay problems. Therefore the reliability and the application range of both numerical schemes are first examined by studying pure Ohmic decay problems in the absence of fluid flow. A cylindrical geometry is chosen with radius $R=1.4$ and height $H=2.6$ which is in accordance with the setting of the VKS experiment. The cylinder is filled with a conductor with diffusivity $\eta=(\mu_0\sigma_0)^{-1}=1$ and relative permeability $\mu_r=1$. Two disks are introduced inside the domain, characterized by thickness $d\in\{0.6, 0.3, 0.1\}$, conductivity σ and permeability μ_r (figure 3). The thickness $d=0.1$ is representative of the VKS impellers but the other d have been tested to study the scaling law with an effective permeability or an effective conductivity and also to estimate the impact of the numerical resolutions.

In a freely decaying system the azimuthal Fourier modes are independent from one another as long as μ_r and σ are axisymmetric. Moreover the axisymmetric mode ($m=0$) can be split into decoupled poloidal (B_r, B_z) and toroidal (B_φ) components which decay independently and exhibit two distinct decay rates. The three components of the magnetic field of each Fourier mode $m\geq1$ are coupled, i.e., the poloidal and toroidal components interact and have the same decay rate when $m\geq1$. The Ohmic decay rates are computed with SFEMaNS by solving an eigenvalue problem using the

ARPACK package. Between 10 to 40 eigenvectors are computed for each azimuthal Fourier mode, and the dominant eigenvector, i.e. the one whose eigenvalue has the largest real part is extracted. Applying the grid-based FV/BEM algorithm, equation (1) is time stepped and the growth (respectively decay) rates are estimated from the time behavior of the magnetic field amplitude. Initial conditions are given by a divergence free random magnetic field which ensures that all possible eigen vectors are excited.

In the following, we limit our examinations to the decay of the axisymmetric mode ($m=0$) and the simplest non-axisymmetric mode, i.e. the ($m=1$)-mode ($B \propto \cos\varphi$).

4.1. *External boundary conditions and field pattern*

A couple of simulations have been performed utilizing vanishing tangential field boundary conditions in order to make comparisons with the vacuum boundary conditions. Figure 4 shows the structure of the field geometry with the container embedded in vacuum (upper panels) and with VTF boundary conditions (lower panels). We observe that the boundary conditions have significant impacts when the conductivity and the permeability are uniform in the whole computational domain. This impact becomes negligible when the disk permeability or conductivity is large enough. More noticeable differences occur when comparing the axisymmetric eigenmode of the magnetic field obtained with high-permeability disks with that obtained with high conductive disks. In the first case (as μ_r increases) the axisymmetric mode changes from a poloidal dominant structure to a toroidal dominant structure (see figure 5 for $d=0.6$). The change of structure occurs irrespective of d around $\mu_r^{\text{eff}} \approx 1.5$, where μ_r^{eff} denotes the effective value for permeability defined by $\mu_r^{\text{eff}} = V^{-1} \int \mu_r(\mathbf{r}) \mathrm{d}V$ (with V the volume of the cylindrical domain). The field structure is dominated by two distinct azimuthal annular structures essentially located within the disks. When the conductivity is large the axial component of the magnetic field dominates and has a slab like structure concentrated around the axis.

A remarkable change in the field structure is obtained when the thickness of the disks is small ($d=0.1$, figures 6 and 7). When μ_r is large the azimuthal component of the field is dominated by two ring like structures centered on the outer part of both disks. The radial field component is concentrated within two highly localized paths on the outer edge of the disk. The axial component is nearly independent from z except close to the disks where the jump conditions require H_z to be very small within the disks. The differences in the field patterns between $d=0.6$ and $d=0.1$ are less significant when the conductivity is large where a torus-like structure of the poloidal field component dominates in all cases (see right panel in figure 7).

Note the equatorial symmetry breaking in the toroidal field when the conductivity is large ($\mu_0\sigma=100$, central column in figure 4). The asymmetry in H_φ results from the occurrence of combined contributions with dipole-like symmetry (even with respect to the equator) and quadrupolar-like symmetry (odd with respect to the equator). Using ARPACK, the SFEMaNS scheme yields decay rates for both symmetries which are close but not equal (the dipole mode always has a larger decay time than the quadrupole mode).

Downloaded By: [Giesecke, Andre] At: 22:12 14 September 2010

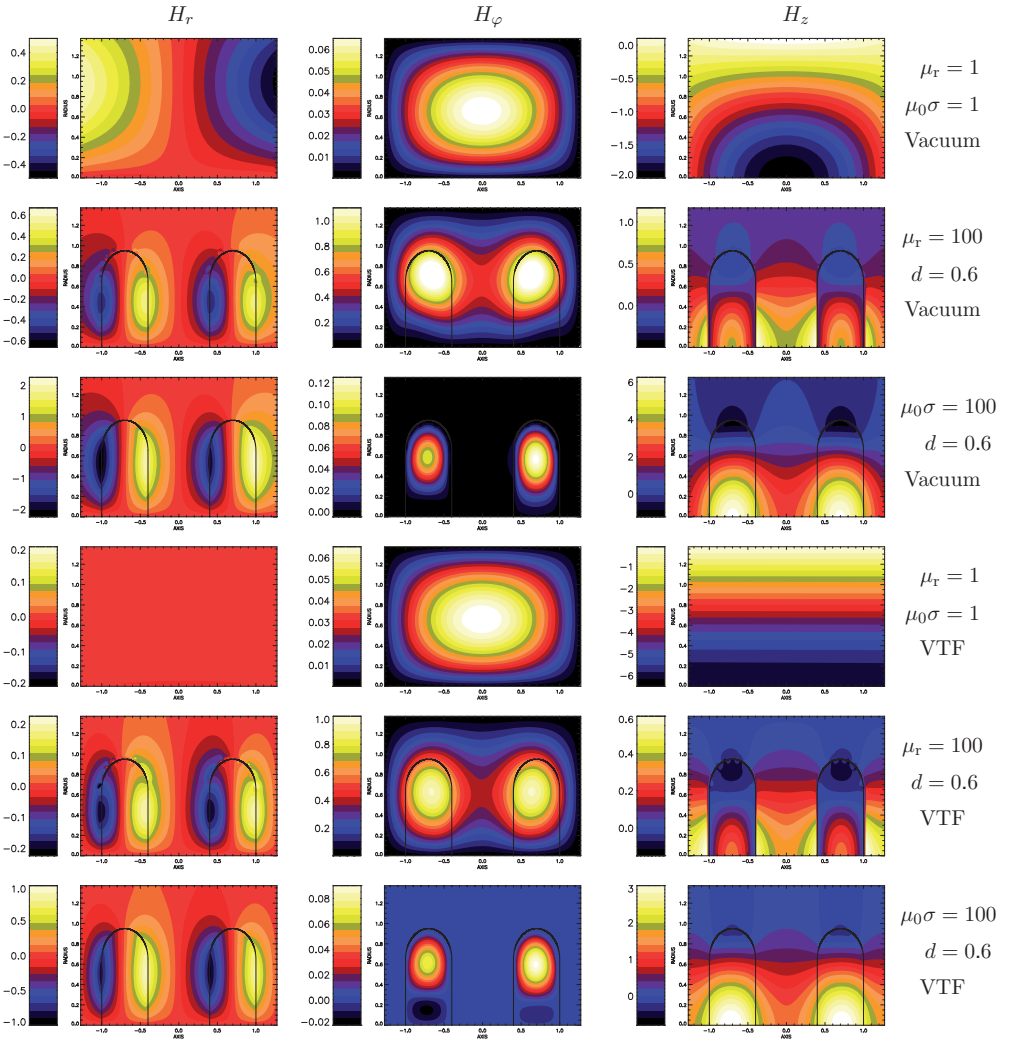

Figure 4. (Color online) Ohmic decay. Axisymmetric eigenmodes of the magnetic field $\mathbf{H} = \mu_r^{-1}\mathbf{B}$ (from left to right: H_r, H_φ, H_z); From top to bottom: $\mu_r = \mu_0\sigma = 1$ (no disks), $\mu_r = 100$, $\mu_0\sigma = 100$ (all with insulating boundary conditions and $d = 0.6$), $\mu_r = \mu_0\sigma = 1$ (no disks), $\mu_r = 100$, $\mu_0\sigma = 100$ (all with vanishing tangential field boundary conditions and $d = 0.6$). Note that the absolute amplitudes denoted by the respective color bars are meaningless and only serve to compare the relative amplitudes of the different components within one case.

4.2. *Decay rates and dominating mode*

The temporal behavior of the magnetic eigenmodes follows an exponential law $B \propto e^{\gamma t}$ where γ denotes the growth or decay rate. Figure 8 shows the magnetic field decay rates for a thick disk ($d = 0.6$) and a thin disk ($d = 0.1$) against μ_r^{eff} (left column) and against σ^{eff} (right column). σ^{eff} denotes the effective values for the conductivity defined similar to μ_r^{eff} (see above) by $\sigma^{\text{eff}} = V^{-1}\int\sigma(\mathbf{r})\mathrm{d}V$. The essential properties of the field behavior can be summarized as follows: The presence of high-permeability/conductivity material

Downloaded By: [Giesecke, Andre] At: 22:12 14 September 2010

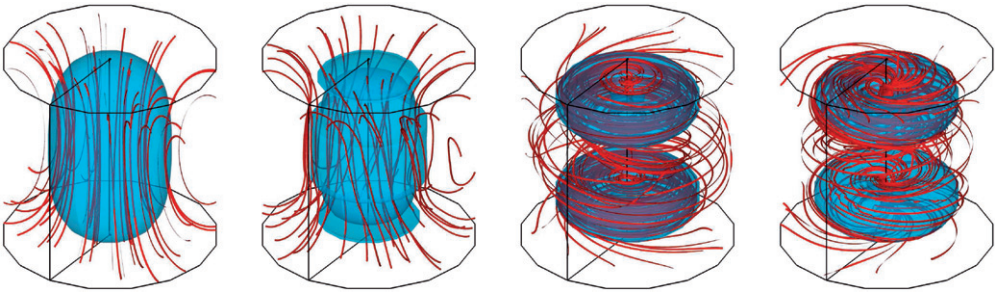

Figure 5. (Color online) Ohmic decay. The blue transparent isosurfaces present the magnetic energy density at 25% of the maximum value and the red fieldlines show the field structure for $d=0.6$ and (from left to right): $\mu_r=1, 2, 10, 100$ (corresponding to $\mu_r^{\rm eff}=1, 1.2, 2.7, 19.5$).

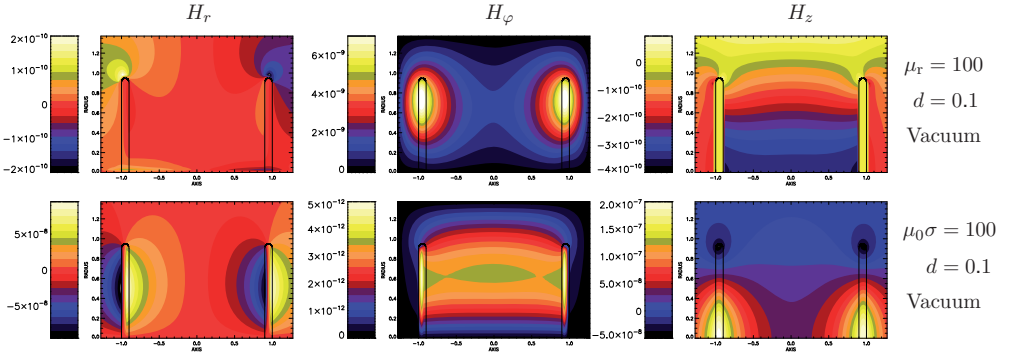

Figure 6. (Color online) Ohmic decay. Axisymmetric field $\mathbf{H}=\mu_r^{-1}\mathbf{B}$ for the thin disk case ($d=0.1$, from left to right: H_r, H_φ, H_z); Top row: $\mu_r=100$, bottom row: $\mu_0\sigma=100$. Insulating boundary conditions. Note that the absolute amplitudes denoted by the respective color bars are meaningless and only serve to compare the relative amplitudes of the different components within one case.

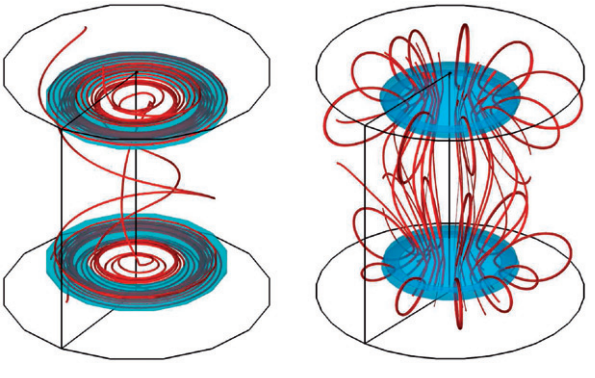

Figure 7. (Color online) Ohmic decay for thin disks ($d=0.1$). Left panel: $\mu_r=100$, right panel: $\mu_0\sigma=100$. The isosurfaces present the magnetic energy density at 25% of its maximum value.

Downloaded By: [Giesecke, Andre] At: 22:12 14 September 2010

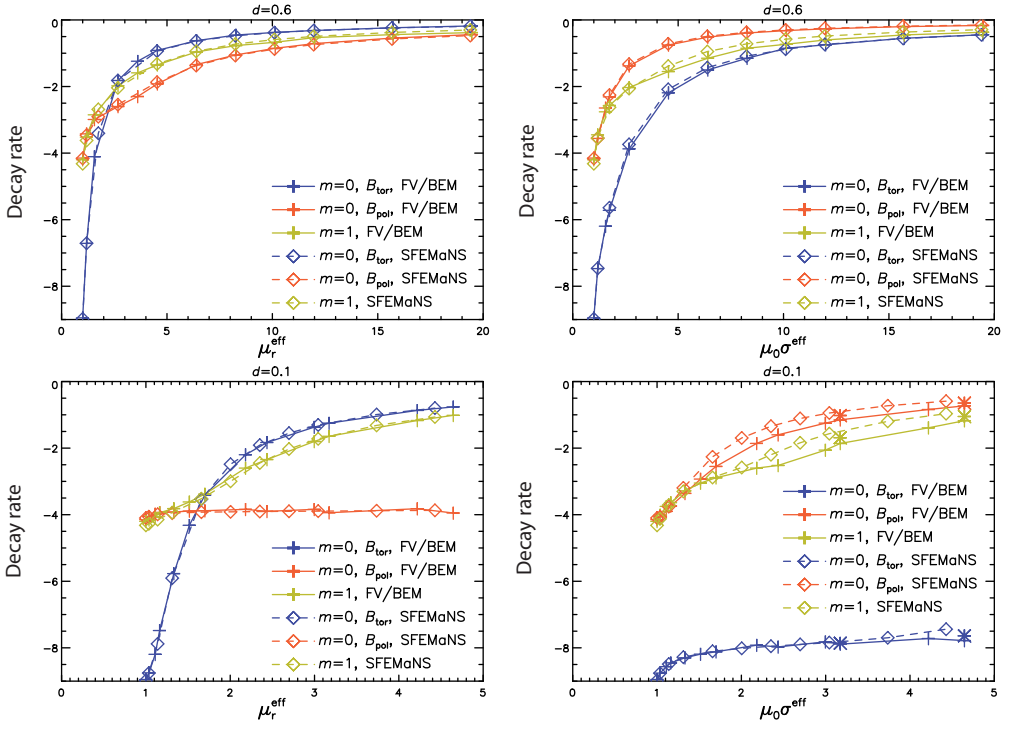

Figure 8. (Color online) Decay rates with vacuum BC against μ_r^{eff} (left column) and against $\mu_0\sigma^{eff}$ (right column) for $d=0.6$ (top row) and $d=0.1$ (bottom row). The solid curves show the results obtained from the hybrid FV/BEM scheme and the dashed curves denote the results from the SFEMaNS scheme. The stars in the lower right panel present the results of a FV/BEM run with higher resolution demonstrating that the FV/BEM algorithm might approach the SFEMaNS data.

enhances axisymmetric and ($m=1$) modes. However, for thin disks the enhancement works selectively for the axisymmetric toroidal field (in case of large μ_r), respectively for the poloidal axisymmetric mode (in case of large σ) and the decay rate of the poloidal (respectively toroidal) field component remains nearly independent of the permeability (respectively conductivity).

Small differences can be observed between the results obtained by the SFEMaNS and FV/BEM algorithms. These are particularly noticeable for the axisymmetric poloidal mode and for the ($m=1$) mode when the disks are thin ($d=0.1$). A couple of simulations with higher resolution in the axial direction (marked by the blue, red and the yellow stars in the lower right panel of figure 8) show that these deviations are most probably the result of the poor resolution of the FV/BEM scheme. Only six mesh points are used to resolve the vertical structure of the disk in FV/BEM whereas SFEMaNS uses 40 mesh points. More systematic discrepancies between both algorithms become obvious by means of the behavior of the decay time τ defined by the reciprocal value of the decay rate (figure 9). For sufficiently large values of μ_r^{eff} (respectively σ^{eff}), τ follows a scaling law $\tau \propto c\mu_r^{eff}$ (respectively $\propto c\sigma^{eff}$) as reported in table 1. For increasing μ_r^{eff} the decay time of the ($m=0$) toroidal mode slightly increases as d decreases whereas the axisymmetric poloidal mode exhibits an opposite behavior. The variation of the decay time with σ^{eff} for the ($m=0$) components (toroidal and poloidal) is the opposite to the

Downloaded By: [Giesecke, Andre] At: 22:12 14 September 2010

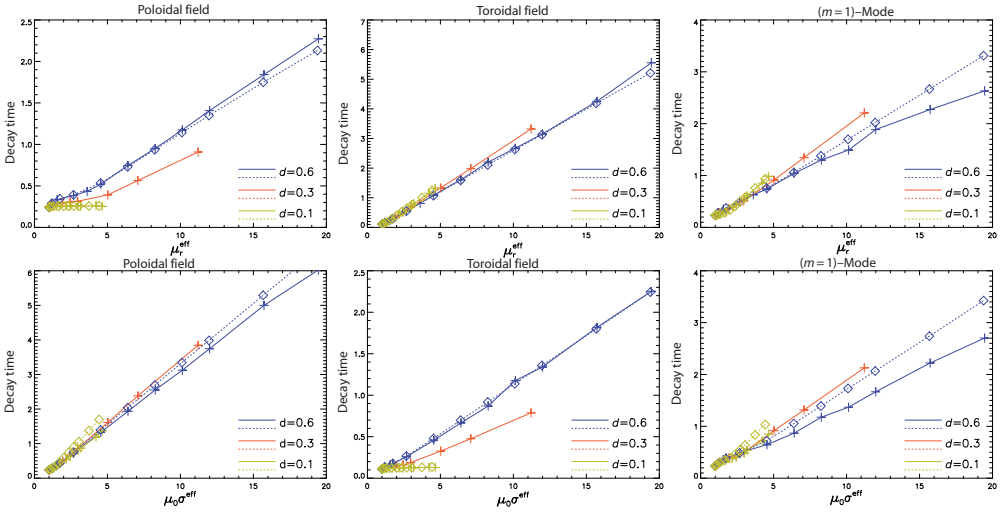

Figure 9. (Color online) Ohmic decay. Decay times against μ_r^{eff} (top row) and against $\mu_0\sigma^{\text{eff}}$ (bottom row) for three disk thicknesses $d=0.6, 0.3, 0.1$ (blue, red, yellow). The solid curves show the results obtained from the hybrid FV/BEM scheme and the dotted curves denote the results from the SFEMaNS scheme.

Table 1. Scaling coefficient c for the decay time as $\tau \propto c\mu_r^{\text{eff}}$ (respectively $c\mu_0\sigma^{\text{eff}}$) for different $m=0$ and $m=1$ modes as indicated (vacuum BC).

	μ_r^{eff}			σ^{eff}			
d	0.6	0.3	0.1	0.6	0.3	0.1	Algorithm
$\tau(B^{\text{tor}}_{m=0})$	0.29	0.32	0.33	0.12	0.07	0.00	FV/BEM
	0.28	–	0.34	0.12	–	0.00	SFEMaNS
$\tau(B^{\text{pol}}_{m=0})$	0.12	0.08	0.00	0.32	0.36	0.33	FV/BEM
	0.11	–	0.00	0.35	–	0.45	SFEMaNS
$\tau(B_{m=1})$	0.12	0.21	0.25	0.14	0.20	0.20	FV/BEM
	0.17	–	0.25	0.18	–	0.28	SFEMaNS

behavior obtained with varying μ_r^{eff}. These variations with respect to d suggest that the decay time scaling law not only depends on the ferromagnetic volume of the impellers but also depends on the geometric constraints associated with the jump conditions (3).

Further evaluation of the discrepancies in the scaling behavior obtained by both numerical schemes is difficult, since it would require doing simulations with larger values for μ_r^{eff} and/or σ^{eff}, which is not possible at the moment without significantly improving the numerical schemes. In particular for the thin disk case ($d=0.1$) the achievable values for μ_r and/or σ are restricted to μ_r^{eff} (respectively $\mu_0\sigma^{\text{eff}}$) $\lesssim 5$ and, with the available data, it is not obvious whether the asymptotic linear scaling has been reached. In any case the absolute values for the decay rates obtained by both algorithms are close, giving confidence that the results imply a sufficiently accurate description of the magnetic field behavior in the presence of non-heterogenous materials.

As already indicated by the marginal differences in the field pattern for both examined boundary conditions, we find no qualitative change in the behavior of the

Downloaded By: [Giesecke, Andre] At: 22:12 14 September 2010

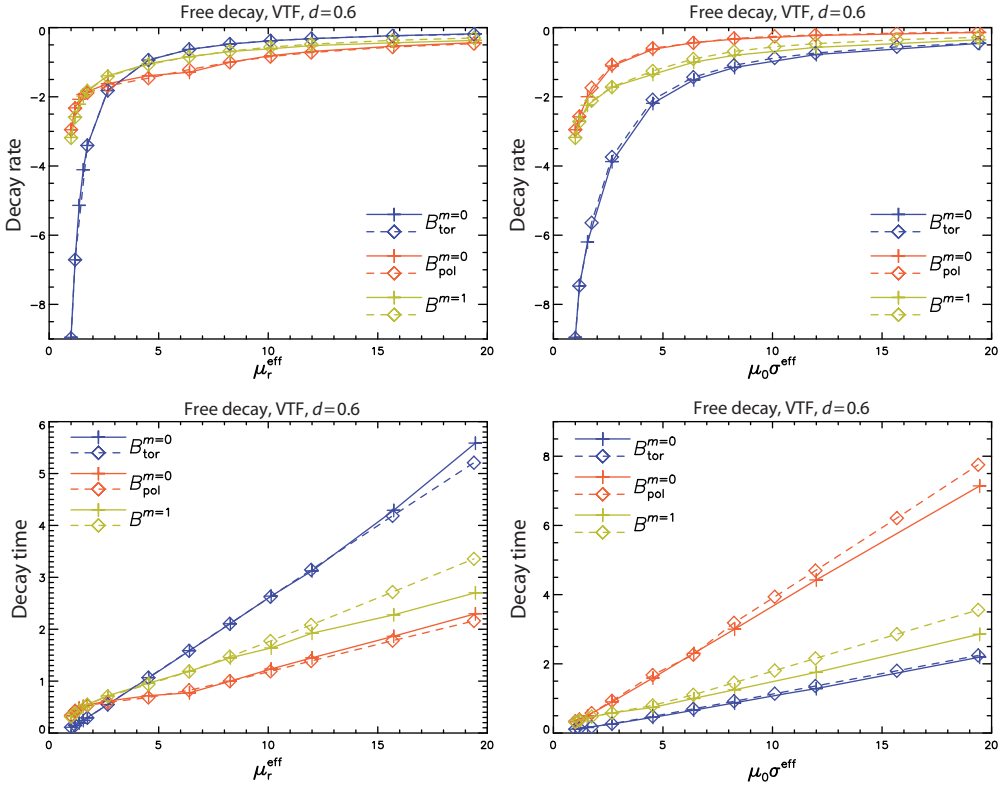

Figure 10. (Color online) Decay rates and decay times against μ_r^{eff} (left column) and against $\mu_0\sigma^{eff}$ (right column) for vanishing tangential fields boundary conditions. $d=0.6$. The solid (dashed) curves denote the results from the FV/BEM (SFEMaNS) scheme.

Table 2. Scaling coefficient c for the decay time as $\tau \propto c\mu_r^{eff}$ for thick disks ($d=0.6$) and VTF boundary conditions.

	μ_r^{eff}	σ^{eff}	
$\tau(B_{m=0}^{tor})$	0.29	0.12	FV/BEM VTF
	0.28	0.12	SFEMaNS VTF
$\tau(B_{m=0}^{pol})$	0.12	0.37	FV/BEM VTF
	0.10	0.42	SFEMaNS VTF
$\tau(B_{m=1})$	0.11	0.14	FV/BEM VTF
	0.17	0.19	SFEMaNS VTF

decay rates or decay times with vacuum boundary conditions or VTF boundary conditions (figure 10). Although for small values of μ_r^{eff} and σ^{eff} the absolute values of the decay rates differ by 30% the scaling behavior of the decay time is nearly independent of the external boundary conditions (table 2). The influence of these boundary conditions is smaller as μ_r increases. Although the decay rates (for the thick disks) differ by approximately 30% when $\mu_r \lesssim 5$ there are nearly no differences in γ for higher values of the permeability. This behavior is less obvious in case of a high

Downloaded By: [Giesecke, Andre] At: 22:12 14 September 2010

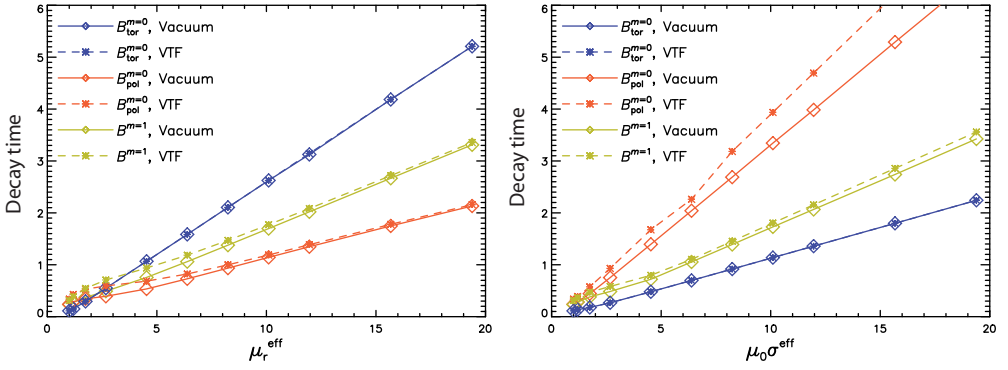

Figure 11. (Color online) Comparison of boundary conditions. Decay times against μ_r^{eff} (left panel) and against $\mu_0\sigma^{\text{eff}}$ (right panel) for vacuum BC (solid curves) and VTF boundary conditions (dashed curves). $d=0.6$. All data results from the SFEMaNS scheme.

Downloaded By: [Giesecke, Andre] At: 22:12 14 September 2010

conductivity disk where the poloidal axisymmetric field exhibits differences in the decay rates of 15% even at the highest available conductivity (figure 11). Note that the axisymmetric toroidal field behaves exactly in the same way for both kinds of boundary conditions because insulating boundary conditions and vanishing tangential field conditions are identical for the axisymmetric part of B_φ.

5. Kinematic dynamo

In the following, the kinematic induction equation is solved numerically with $\mathrm{Rm}>0$ in order to examine whether the behavior of the magnetic field obtained in the free decay regime is maintained when interaction with a mean flow is allowed. To approximately mimic the VKS experiment, we apply the so called MND-flow (Marié *et al.* 2006) given by

$$\begin{aligned} u_r(r,z) &= -(\pi/H)\cos(2\pi z/H)r(1-r)^2(1+2r),\\ u_\varphi(r,z) &= 4\epsilon r(1-r)\sin(\pi z/H),\\ u_z(r,z) &= (1-r)(1+r-5r^2)\sin(2\pi z/H), \end{aligned} \tag{30}$$

where $H=1.8$ denotes the distance between the impeller disks and ϵ measures the ratio between toroidal and poloidal component of the velocity (here, $\epsilon=0.7259$ is chosen following previous work, e.g. Stefani *et al.* 2006). The flow magnitude is characterized by the magnetic Reynolds number which is defined as

$$\mathrm{Rm}=\mu_0\sigma_0 U_{\max} R, \tag{31}$$

where $U_{\max}$ is the maximum of the flow velocity and σ_0 denotes the fluid conductivity. Figure 12 shows the structure of the velocity field where equations (30) are applied only in the region between the two impellers. The flow active region with radius $R=1$ (corresponding to 20.5 cm in the experiment) is surrounded by a layer of stagnant fluid with a thickness of $0.4R$ (the side layer) which significantly reduces Rm^c

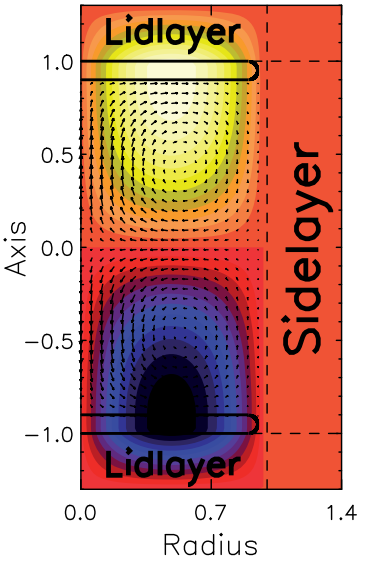

Figure 12. (Color online) Structure of the prescribed axisymmetric velocity field. The color coded pattern represents the azimuthal velocity and the arrows show the poloidal velocity field. The black solid lines represent the shape of the impeller disk.

Downloaded By: [Giesecke, Andre] At: 22:12 14 September 2010

(Stefani *et al.* 2006). In the domain of the impellers a purely azimuthal velocity is assumed given by the azimuthal velocity of the MND flow (see equation (30)) at $z = \pm H/2$. A so-called lid layer is added behind each impeller disk. A purely rotating flow is assumed within these lid layers, and it is modeled by a linear interpolation along the z-axis between the azimuthal velocity at the outer side of the impeller disk and zero at the end cap of the cylindrical domain. Here we limit our examinations to disks with a height $d = 0.1$. Note that the impellers are modeled only by the permeability and/or conductivity distribution and no particular flow boundary conditions are enforced on the (assumed) interface between the impellers and the fluid. This setup is comparable to the configuration in Giesecke *et al.* (2010b) except that we now assume that permeability and conductivity are axisymmetric.

Figure 13 shows the growth rates for the $(m = 1)$ mode for different magnetic Reynolds numbers. Compared to the free decay, we obtain a remarkable distinct behavior of the growth rate if induction from a mean flow is added. High permeability disks together with $\mathrm{Rm} > 0$ enhance the $(m = 1)$ mode when compared to the case $\mu_\mathrm{r} = 1$ resulting in a non-negligible impact on the critical magnetic Reynolds number for the onset of dynamo action (of this mode): Rm^c is reduced from around 76 at $\mu_\mathrm{r} = 1$ to Rm^c around 55 at $\mu_\mathrm{r} = 100$. For $\mu_\mathrm{r} \gg 1$, the behavior of Rm^c indicates a saturation around $\mathrm{Rm}^\mathrm{c} \approx 55$ which is still above the highest achievable experimental value of 50. The enhancement of the $(m = 1)$ mode for $\mathrm{Rm} \neq 0$ is weaker compared to the Ohmic decay (green curve in left panel of figure 13). An opposite behavior is obtained for a high-conducting disk where a reduction of the $(m = 1)$ growth rate is obtained (see right panel of figure 13).

In both cases the $(m = 1)$ decay rate remains independent of μ_r (respectively σ) for values exceeding approximately $\mu_\mathrm{r} \approx 20$ (or $\mu_0 \sigma \approx 20$). The critical magnetic Reynolds

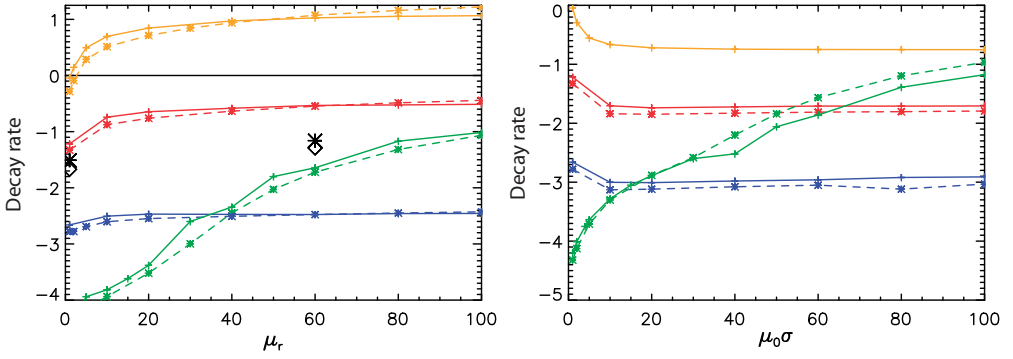

Figure 13. Growth rates for the MND flow driven dynamo against μ_r (left panel) and against $\mu_0\sigma$ (right panel). Solid curves denote data obtained from the FV/BEM scheme, dashed curves denote the results from the SFEMaNS scheme. The green, blue, red, yellow colors denote the cases $\mathrm{Rm} = 0, 30, 50, 70$. The black stars in the left panel show the results for the SMND flow at $\mathrm{Rm} = 50$ (see text) as reported in table 3.

Table 3. Decay rate for $m = 1$ mode for 2 flows MND and a similar flow with slightly modified (smoothed) radial velocity component (SMND).

$m = 1$, $Rm = 50$	$\mu_r = 1$ (FV/BEM)	$\mu_r = 1$ (SFEMaNS)	$\mu_r = 60$ (FV/BEM)	$\mu_r = 60$ (SFEMaNS)
MND	−1.218	−1.327	−0.550	−0.655
SMND	−1.51	−1.667	−1.16	−1.291

number has also been computed for a different set-up with the flow restricted to the bulk region: $0 \le r \le 1.4$, $-0.9 \le z \le 0.9$ with VTF conditions applied at the boundary of this region. We obtained $\mathrm{Rm}^c = 39$ in this case. Note that this pseudo-vacuum set-up under-estimates the threshold by more than 30% when compared to $\mathrm{Rm}^c = 55$ in the limit $\mu_r \gg 1$. This confirms that a realistic description of the soft iron impellers is crucial to get correct estimates.

The robustness of the results reported above exhibits a rather delicate dependence of the field behavior on the details of the flow distribution, in particular on the flow in the lid layers. Beside the dynamo killing influence of the lid flow (Stefani *et al*. 2006) this is also true for the radial flow in the vicinity of the inner side of the disks. In order to estimate the relative impact of velocity jumps on the two codes, some simulations have been performed by smoothing the radial component of the velocity at the transition between the bulk of the domain and the impeller disk (where $u_r = 0$). The resulting decay rates at $\mathrm{Rm} = 50$ (black stars in the left panel of figure 13 and table 3) are slightly different at $\mu_r = 1$ but the difference is more significant for $\mu_r = 60$.

6. Conclusions

In addition to its well-recognized effects in magnetostatics, experimental dynamos have shown that soft-iron material may also find important applications in the field of magnetohydrodynamics. For instance, at least one of the two impellers of the Cadarache experiment must be made of soft iron and must rotate in order to achieve dynamo action (F. Daviaud, private communication). This unexplained fact raises the

Downloaded By: [Giesecke, Andre] At: 22:12 14 September 2010

question as to whether the role of this material is only to lower the critical magnetic Reynolds number in the domain of experimental feasibility or if the dynamo mechanism is fundamentally different when the conducting medium is no longer homogeneous. This issue can be addressed numerically in principle . However, to face such problems with heterogenous domains, specific algorithms must be implemented and validated. This was the aim of the present study. Our comparative runs of Ohmic decay problems proved, in practice, to be extremely useful to optimize both codes and to select some numerical coefficients occurring in the algorithms (such as in penalty terms).

The problems which have been successively presented above are standard in MHD, but we were forced to reduce the dimension of the parameter space to configurations more or less related to the Cadarache experiment, where the impellers may be treated as disks in a conducting flow bounded by a cylinder of a given aspect ratio. We have thus considered axisymmetric domains only (see Giesecke *et al.* (2010b) for non-axisymmetric cases), and azimuthal modes of low order ($m = 0$ and 1).

Downloaded By: [Giesecke, Andre] At: 22:12 14 September 2010

We have first studied Ohmic decay problems, with disk impellers of various thicknesses to investigate scaling laws and the impact of the spatial resolution. The effects of internal assemblies of high-permeability material within the fluid container are different from those of an enhanced, but homogeneous fluid permeability because of inner boundary conditions for the magnetic field (in case of high-permeability material), and for the electric field/current (in case of conductivity jumps). In the free decay problem with thin high-permeability disks a selective enhancement of the axisymmetric toroidal field and the ($m = 1$) mode is observed whereas the axisymmetric poloidal field component is preferred in case of high conductive disks.

We have also shown that pseudo-vacuum boundary conditions, which are easier to implement on the cylinder walls than the jump conditions on the impellers, have only a slight influence on the decay rates. The impact of the outer container boundaries on the field behavior is limited to a shift of the decay/growth rates. This is surprising, insofar as pseudo vacuum boundary conditions resemble the conditions that correspond to an external material with infinite permeability. Nevertheless, the presence of high-permeability/conductivity disks within the liquid hides the influence of outer boundary conditions, and the simplifying approach applying vanishing tangential field conditions at the end caps of the cylinder in order to mimic the effects of the high-permeability disks in the VKS experiment (Gissinger *et al.* 2008) is not sufficient to describe the correct field behavior. The consideration of impeller disks with (large but finite) permeability remains indispensable in order to describe the influence of the material properties.

For completeness, we have also considered domains with enhanced conductivity. From the experimental point of view the utilization of disks with a conductivity that is 100 times larger than the conductivity of liquid sodium remains purely academic. Nevertheless, the simulations show a crucial difference between heterogeneous permeabilities and conductivities: even if these two quantities may appear in the definition of an effective Reynolds number $\mathrm{Rm}^{\mathrm{eff}} = \mu_0 \mu_{\mathrm{r}}^{\mathrm{eff}} \sigma^{\mathrm{eff}} UL$, they do not play the same role and they select different geometries of the dominant decaying mode. It is not only a change of magnetic diffusivity that matters.

We have considered kinematic dynamo action, using analytically defined flows in accordance with the setting of the VKS mean flow. Since these flows and the variation of μ and σ are axisymmetric, the azimuthal modes are decoupled. An important Fourier mode is the ($m = 1$) mode which will be excited eventually through dynamo action.

We have shown that our codes give comparable growth rates for this azimuthal mode. We have also examined the decay rate of the ($m=0$) magnetic field in the presence of soft iron impellers and the axisymmetric MND flow. Since convergence of results is not achieved in all the cases considered, this comparative study is still in progress and it has thus not been included in the present article. We recall that the main surprise of the Cadarache experiment was perhaps the occurrence of the mode ($m=0$), which pointed out the possible role of the non-axisymmetric flow fluctuations. Non-axisymmetric velocity contributions might be considered in terms of an α-effect as it has been proposed in Pétrélis *et al.* (2007) and Laguerre *et al.* (2008a,b). Preliminary examinations applying simple α-distributions are presented in Giesecke *et al.* (2010a,b). However, there is still a lack of knowledge on the details and physical justification of a precise α-distribution which requires a nonlinear hydrodynamic code. The questions related to this empirical fact represent a main issue of the experimental and numerical approaches of the fluid dynamo problem and deserve a dedicated study. Our axisymmetric model is not intended to explain the main features of the VKS experiment, which are the dominating axisymmetric field mode and the surprising low critical magnetic Reynolds number of $\mathrm{Rm} \approx 32$. However, our results give a hint why the ($m=1$) mode remains absent in the experiment.

A source term on the $m=0$ mode appears when the flow axisymmetry is broken. Although the relative amplitude of this source cannot be discussed here, we note that the decay time of the ($m=0$) toroidal mode becomes the largest when the effective permeability is high enough (see, e.g. figure 8). It may thus appear as the dominant mode of the dynamo, as it seems to be observed in the VKS experiment. Stated otherwise, the impact of soft-iron impellers on the critical magnetic Reynolds number of the ($m=1$)-mode could be rather low (decrease from ~ 76 to ~ 55 in the MND case) and could remain unobservable, while it could be strong for the ($m=0$) mode (down to 32 in the VKS geometry) when conjugated with a slight departure from axisymmetry of the flow. Numerical evidences for this picture require the consideration of non-axisymmetric velocity contributions, either in terms of vortices such as, e.g. observed in water experiments by de la Torre and Burguete (2007) or applying a physically established profile of an α-effect.

Downloaded By: [Giesecke, Andre] At: 22:12 14 September 2010

Acknowledgements

We gratefully acknowledge the financial support from Deutsche Forschungsgemeinschaft (DFG) in frame of the Collaborative Research Center (SFB) 609 and from European Commission under contract 028679. The computations using SFEMaNS were carried out on the IBM SP6 computer of Institut du Développement et des Ressources en Informatique Scientifique (IDRIS) (project # 0254).

References

Avalos-Zuñiga, R. and Plunian, F., Influence of inner and outer walls electromagnetic properties on the onset of a stationary dynamo action. *Eur. Phys. J. B* 2005, **47**, 127–135.

Avalos-Zuñiga, R., Plunian, F. and Gailitis, A., Influence of electromagnetic boundary conditions onto the onset of dynamo action in laboratory experiments. *Phys. Rev. E* 2003, **68**, 066307.

Downloaded By: [Giesecke, Andre] At: 22:12 14 September 2010

Bonito, A. and Guermond, J.-L., Approximation of the eigenvalue problem for time harmonic Maxwell systems by continuous Lagrange finite elements. *Math. Comp.* 2010 (in press).

Busse, F.H. and Wicht, J., A simple dynamo caused by conductivity variations. *Geophys. Astrophys. Fluid Dyn.* 1992, **64**, 135–144.

Costabel, M., A coercive bilinear form for Maxwell's equations. *J. Math. Anal. Appl.* 1991, **157**, 527–541.

de la Torre, A. and Burguete, J., Slow dynamics in a turbulent von Kármán swirling flow. *Phys. Rev. Lett.* 2007, **99**, 054101.

Dobler, W., Frick, P. and Stepanov, R., Screw dynamo in a time-dependent pipe flow. *Phys. Rev. E* 2003, **67**, 056309.

Frick, P., Khripchenko, S., Denisov, S., Sokoloff, D. and Pinton, J.F., Effective magnetic permeability of a turbulent fluid with macroferroparticles. *Eur. Phys. J. B* 2002, **25**, 399–402.

Giesecke, A., Nore, C., Plunian, F., Laguerre, R., Ribeiro, A., Stefani, F., Gerbeth, G., Leorat, J. and Guermond, J., Generation of axisymmetric modes in cylindrical kinematic mean-field dynamos of VKS type. *Geophys. Astrophys. Fluid Dyn.* 2010a, **104**, 249–271.

Giesecke, A., Stefani, F. and Gerbeth, G., Kinematic simulations of dynamo action with a hybrid boundary-element/finite-volume method. *Magnetohydrodynamics* 2008, **44**, 237–252.

Giesecke, A., Stefani, F. and Gerbeth, G., Role of soft-iron impellers on the mode selection in the von-Kármán–sodium dynamo experiment. *Phys. Rev. Lett.* 2010b, **104**, 044503.

Gissinger, C., Iskakov, A., Fauve, S. and Dormy, E., Effect of magnetic boundary conditions on the dynamo threshold of von Kármán swirling flows. *Europhys. Lett.* 2008, **82**, 29001.

Guermond, J.L., Laguerre, R., Léorat, J. and Nore, C., Nonlinear magnetohydrodynamics in axisymmetric heterogeneous domains using a Fourier/finite element technique and an interior penalty method. *J. Comput. Phys.* 2009, **228**, 2739–2757.

Guermond, J.L., Laguerre, R., Léorat, J. and Nore, C., An interior penalty Galerkin method for the MHD equations in heterogeneous domains. *J. Comput. Phys.* 2007, **221**, 349–369.

Haber, E. and Ascher, U.M., Fast finite volume simulation of 3d electromagnetic problems with highly discontinuous coefficients. *SIAM J. Sci. Comput.* 2001, **22**, 1943–1961.

Iskakov, A.B., Descombes, S. and Dormy, E., An integro-differential formulation for magnetic induction in bounded domains: boundary element-finite volume method. *J. Comp. Phys.* 2004, **197**, 540–554.

Iskakov, A.B. and Dormy, E., On magnetic boundary conditions for non-spectral dynamo simulations. *Geophys. Astrophys. Fluid Dyn.* 2005, **99**, 481–492.

Jackson, J.D., *Classical Electrodynamics*, 2nd ed., 1975 (New York: Wiley), 1975.

Laguerre, R., Nore, C., Ribeiro, A., Léorat, J., Guermond, J. and Plunian, F., Impact of impellers on the axisymmetric magnetic mode in the VKS2 dynamo experiment. *Phys. Rev. Lett.* 2008a, **101**, 104501.

Laguerre, R., Nore, C., Ribeiro, A., Léorat, J., Guermond, J. and Plunian, F., Erratum: Impact of impellers on the axisymmetric magnetic mode in the VKS2 dynamo experiment [*Phys. Rev. Lett.* 2008, **101**, 104501]. *Phys. Rev. Lett.* 2008b, **101**, 219902.

Lowes, F.J. and Wilkinson, I., Geomagnetic dynamo: a laboratory model. *Nature* 1963, **198**, 1158–1160.

Lowes, F.J. and Wilkinson, I., Geomagnetic dynamo: an improved laboratory model. *Nature* 1968, **219**, 717–718.

Marié, L., Normand, C. and Daviaud, F., Galerkin analysis of kinematic dynamos in the von Kármán geometry. *Phys. Fluids* 2006, **18**, 017102.

Monchaux, R., *et al.*, Generation of a magnetic field by dynamo action in a turbulent flow of liquid sodium. *Phys. Rev. Lett.* 2007, **98**, 044502.

Pétrélis, F., Mordant, N. and Fauve, S., On the magnetic fields generated by experimental dynamos. *Geophys. Astrophys. Fluid Dyn.* 2007, **101**, 289–323.

Roberts, P.H., Glatzmaier, G.A. and Clune, T.L., Numerical simulation of a spherical dynamo excited by a flow of von Kármán type. *Geophys. Astrophys. Fluid Dyn.* 2010, **104**, 207–220.

Stefani, F., Giesecke, A. and Gerbeth, G., Numerical simulations of liquid metal experiments on cosmic magnetic fields. *Theor. Comp. Fluid Dyn.* 2009, **23**, 405–429.

Stefani, F., Xu, M., Gerbeth, G., Ravelet, F., Chiffaudel, A., Daviaud, F. and Leorat, J., Ambivalent effects of added layers on steady kinematic dynamos in cylindrical geometry: application to the VKS experiment. *Eur. J. Mech. B* 2006, **25**, 894–908.

Stone, J.M. and Norman, M.L., ZEUS-2D: a radiation magnetohydrodynamics code for astrophysical flows in two space dimensions: Part I – the hydrodynamic algorithms and tests. *Astrophys. J. Supp.* 1992a, **80**, 753–790.

Stone, J.M. and Norman, M.L., ZEUS-2D: a radiation magnetohydrodynamics code for astrophysical flows in two space dimensions: Part II. The magnetohydrodynamic algorithms and tests. *Astrophys. J. Supp.* 1992b, **80**, 791.

Verhille, G., Plihon, N., Bourgoin, M., Odier, P. and Pinton, J., Induction in a von Kármán flow driven by ferromagnetic impellers. *New J. Phys.* 2010, **12**, 033006.

Ziegler, U., A three-dimensional Cartesian adaptive mesh code for compressible magnetohydrodynamics. *Comp. Phys. Commun.* 1999, **116**, 65–77.